

Impregnation of microporous SDC scaffold as stable Solid Oxide Cell BSCF-based air electrode

Antonio María Asensio^{1*}, Davide Clematis¹, Massimo Viviani², M. Paola Carpanese^{1,2,*}, Sabrina Presto², Davide Cademartori¹, Pere L. Cabot³, Antonio Barbucci^{1,2}

1 Department of Civil, Chemical and Environmental Engineering (DICCA), Università di Genova, Via all'Opera Pia 15, 16145 Genova, Italy

2 Institute of Condensed Matter Chemistry and Technology for Energy (ICMATE), National Research Council (CNR), c/o DICCA-UNIGE, Via all'Opera Pia 15, 16145 Genova, Italy

3 Laboratori D'Electroquímica Dels Materials I Del Medi Ambient, Departament de Química Física, Facultat de Química, Universitat de Barcelona, Martí I Franquès 1-11, Barcelona, 08028, Spain

*Corresponding authors: antoniomaria.asensio@edu.unige.it
carpanese@unige.it

Keywords: Solid Oxide Cells, Oxygen Electrode, BSCF, SDC porous backbone, infiltration

ABSTRACT

Barium strontium cobaltite-ferrite ($\text{Ba}_{1-x}\text{Sr}_x\text{Co}_y\text{Fe}_{1-y}\text{O}_{3-\delta}$, BSCF) is a widely studied mixed ionic-electronic conductor material for air electrode in solid oxide cells (SOC). Despite having excellent features, due to fast oxygen surface exchange and oxygen bulk diffusion, it lacks long-term stability. Electrode/electrolyte thermal expansion coefficient (TEC) mismatch and structural instability at temperature lower than 900 °C are responsible for the increase of electrode polarization which becomes a crucial issue for the long-term stability.

In this work, SOC stability was studied by adding a thin porous samarium-doped ceria (SDC) backbone on top of the dense SDC electrolyte. The porous SDC backbone was then infiltrated by precursor nitrates to obtain a $\text{Ba}_{0.5}\text{Sr}_{0.5}\text{Co}_{0.8}\text{Fe}_{3-\delta}$ composition. The SEM investigation showed a nano-sized BSCF-based layer covering the backbone structure. In addition, symmetrical cells were studied in the 400-700 °C temperature range under anodic and cathodic polarization showing unexpected behavior associated to the electrode microstructure. The modified electrode synergistically enhanced ORR and OER by showing no oxygen vacancies clustering which induces a higher polarization resistance. Ageing procedure was performed for over 120 hours at 600 °C under switched current load of $\pm 0.2 \text{ A}\cdot\text{cm}^{-2}$. The prepared system showed high stability coupled with remarkable electrocatalytic performance and good mechanical properties.

INTRODUCTION

Reaching the ambitious net-zero greenhouse gas emissions objective by 2050 will require the use of several cost-effective new technologies for energy management.

This objective is at the heart of the World Green Deal in line with the EU's commitment to global climate action under the Paris Agreement [1, 2].

With the widespread diffusion of renewable energy sources, the conversion of excess power into fuels and chemicals (P2F/P2G) is considered one of the most promising schemes in the future energy scenario.

Renewable sources are more and more exploited, but further room for their applicability relies on energy levelling systems, able to balance their intrinsic intermittent nature.

Although solid oxide cells (SOC) are the least mature technology, their unique features could provide a significant contribution towards the levelling of the energy costs and the health of our world society [3].

In this framework and with the current energy and climate scenario, the potential impact of SOC-systems is unquestionable.

Due to the good results from the scientific and technological community on Solid Oxide Fuel Cells, also their operation in reverse operating mode is becoming very attractive in order to comply with the new energy scheme by a very effective system.

Moreover, SOC can be used in many different applications, e.g. energy harvester in electrolysis and co-electrolysis mode (SOEC), power generation in fuel cell mode (SOFC) or as an electrochemical Air Separation Unit (eASU). Such cells usually operate at high temperatures (800 °C), with the advantage to have very active electrocatalysis not dependent on the use of critical raw materials. On the other hand, this operating

temperature is responsible for material instability and, therefore, fast system degradation rates. The current SOC trend focuses on decreasing the operating temperature to 500-700 °C, aiming at the mitigation of the negative effects of thermal cycles on system long lasting reliability. Obviously, the lowering of the operating temperature also reduces the electrode kinetics. Particularly sensitive to this aspect is the kinetics of the oxygen reaction (OR) at the air electrode, which has a big impact on the overall system losses. As a consequence, the key to enable SOC future advancements for their deployment is the technology innovation with the development of novel materials and microstructures with enhanced electrocatalytic activity and stability [4, 5]. In recent years, several new materials and electrode structures have been proposed. The most promising air electrode materials in SOC are represented by cobaltite-ferrites and manganites with perovskite structure ABO_3 with mixed ionic and electronic conduction (MIEC). $Ba_{0.5}Sr_{0.5}Co_{0.8}Fe_{0.2}O_{3-\delta}$ (BSCF) is among the most studied MIEC materials for this application, being very active toward the oxygen evolution reaction (OER) and the oxygen reduction reaction (ORR). This is due to its high oxygen vacancies concentration and fast oxygen diffusion rate, with much larger values than other perovskites [6-8]. However, BSCF is also characterized by electrode degradation due to the mismatch between the thermal expansion coefficient (TEC) of the electrocatalyst and the typical electrolytes, which leads to the electrode delamination [9]. BSCF phase transition from cubic to hexagonal, with the latter poor-performing towards the oxygen reaction, is a further issue [10]. Therefore, several research groups are proposing solutions to gain material and electrode stability by i) changing the material inner cell

structure [11], ii) the addition of stabilizing doping elements [12] and iii) tuning the electrode microstructure.

In terms of microstructure, it has been proved that it is one of the key points governing the oxygen reduction in SOFC cathodes [13]. In fact, it is well known that material processing is often the key to transfer material intrinsic properties to real working systems. A wrong process may overshadow positive characteristics that the material intrinsically holds. Furthermore, an appropriate context or framework could bring up unexpected material performance. Particle size, distribution, morphology or changes in the interfaces may be some of the aspects that are strictly related to the material resulting behavior. The infiltration technique allows to tune the electrode microstructure while maintaining a large surface area, and therefore, potentially enhance the electrode performance [14].

In this paper, we want to focus on the electrode architecture as a central key point towards the fruitful exploitation of the material properties. At the best of the authors knowledge this work reports an original investigation on the combination of electrode architecture, electrocatalyst synthesis and deposition process opening a promising way towards a robust, active and stable IT-SOC reversible BSCF-based air electrode.

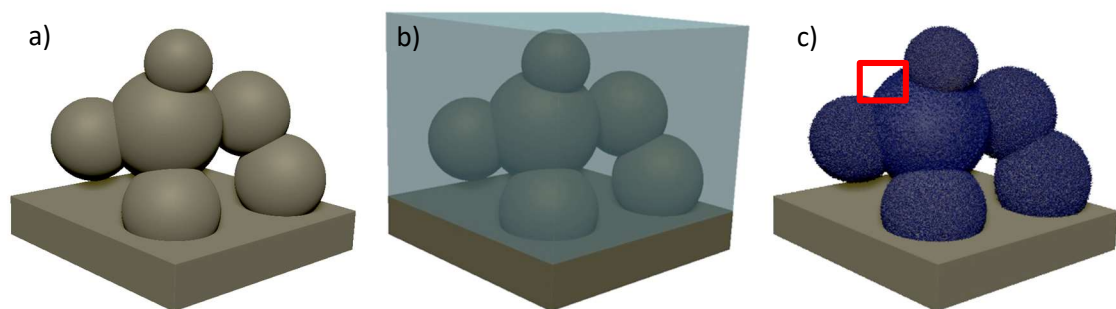
EXPERIMENTAL

The system under study is an electrolyte supported half-cell. The architecture of the air electrode is designed to include the active electrocatalyst in a 15 μm porous Samaria Doped Ceria (SDC) backbone, which is the material also employed for the dense electrolyte. This porous SDC backbone is screen printed on both sides of the dense

electrolyte and is the scaffold of the composite electrode. Indeed, it hosts the electrocatalyst thanks to the infiltration of BSCF precursors for in-situ electrocatalyst synthesis.

This air electrode feature offers the advantages of having a monolithic structure of the electrolyte/electrode interface, which helps both to improve the mechanical strength of the system without penalizing the performance and to creates tiny and homogeneously dispersed particles of the electrocatalyst during infiltration.

The electrolyte backbone preparation and electrocatalyst infiltration are detailed in the following paragraphs and graphically summarized in **Figure 1** Scheme showing the infiltration process: a) A porous electrolyte backbone is screen printed on top of the green supporting electrolyte pellet; b) Precursors infiltration; c) Heat treatment which forms the desired electrocatalyst achieving an active thin-film coating; d) Cross-section showing the oxygen reaction and transport through the whole electrode architecture..



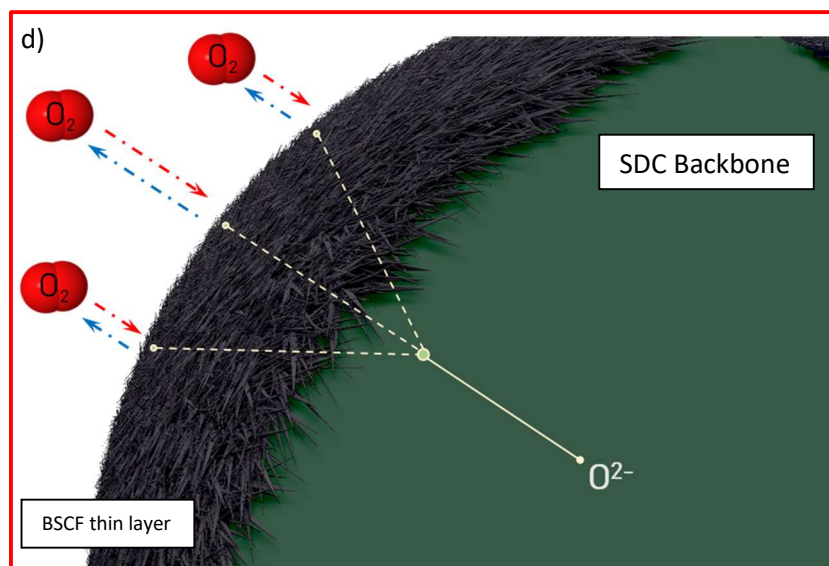


Figure 1 Scheme showing the infiltration process: a) A porous electrolyte backbone is screen printed on top of the green supporting electrolyte pellet; b) Precursors infiltration; c) Heat treatment which forms the desired electrocatalyst achieving an active thin-film coating; d) Cross-section showing the oxygen reaction and transport through the whole electrode architecture.

Fabrication of dense electrolyte and porous electrolyte backbone

The porous SDC backbone as well as the dense electrolyte were fabricated from $\text{Ce}_{0.8}\text{Sm}_{0.2}\text{O}_{2-\delta}$ (Fuel Cell Materials, USA) powders. The electrolyte and the backbone structure, that would later become part of the composite electrode, were processed in one step, thus obtaining a symmetrical cell. At first, the green pellet electrolyte was obtained by uniaxial cold pressing at 40 MPa. On top of the green pellet a thin layer of SDC and spherical graphite as pore former (Sigma-Aldrich, 2-4 μm), corresponding to a 60:40 volume ratio of SDC to graphite, was deposited. Alpha-terpineol was added to the mixture to obtain the suitable ink rheology for screen-printing. The mixture of SDC and graphite was firstly ball-milled with water for 48 hours and freeze-dried for 24 hours in order to remove the solvent and maintain a good dispersion of the components. The symmetrical cell was then sintered at 1450°C for 5 hours in air, with a heating rate of 1

$^{\circ}\text{C min}^{-1}$ leading to dense pellets with 25 mm diameter and a robust porous backbone structure of 6 mm in diameter which after the infiltration would become the electrode area.

To avoid any artefacts during the electrochemical characterization due to possible working electrode (WE) and counter electrode (CE) misalignment, the thickness of the dense electrolyte was equal to 3 mm, in agreement with the indications reported by other works [15].

BSCF infiltration into the porous backbone

The BSCF precursor solution was composed of stoichiometric amounts of $\text{Ba}(\text{NO}_3)_2$ (99%), $\text{Sr}(\text{NO}_3)_2$ (99%), $\text{Co}(\text{NO}_3)_2 \cdot 6 \text{H}_2\text{O}$ (99%) and $\text{Fe}(\text{NO}_3)_3 \cdot 9 \text{H}_2\text{O}$ (98%) (Sigma-Aldrich), according to the formula $\text{Ba}_{0.5}\text{Sr}_{0.5}\text{Co}_{0.8}\text{Fe}_{0.2}\text{O}_{3-\delta}$. The precursors were dissolved in deionized water with a total concentration of 0.3 M and 1.5 wt.% Triton X-100 was added as non-ionic surfactant to improve the solid surface wettability. Different loadings (3, 4, 5 μL of the 0.3 M nitrate solution) were infiltrated into the SDC porous backbone by repeated cycles of 1 μL each. Vacuum was used to facilitate the penetration of the solution into the porous backbone after each infiltration. The 0.3 M solution was chosen in order to be close to the solubility limit of BaNO_3 . On the other hand, this solution has a good fluidity to ensure a proper penetration into the entire porous structure [16].

Three sets of symmetrical cells were prepared with the precursor solution resulting in 10, 15 and 20 wt.% load respectively of BSCF into the overall electrode.

In order to obtain a three-electrode configuration the symmetric half-cells were implemented with a thin ring reference electrode (RE) of commercial BSCF (Treibacher,

Austria) powder deposited concentrically to the WE by means of slurry coating using a mask and a blade. The distance of the RE was kept sufficient to avoid distorted current lines that could generate artefacts [17]. The samples were calcined at 850 °C for 2 hours with a 4 °C·min⁻¹ temperature ramp rate.

Morphological and structural characterization

The analysis of the morphology of the electrolyte backbone and the result of the electrocatalyst infiltration was carried out through Scanning Electron Microscopy (Phenom *ProX*), implemented by Energy-Dispersive X-ray spectroscopy (EDXS).

Structural analysis of the synthesized electrocatalyst was performed by X-ray diffraction (PANalytical, X'Pert PRO MPD alpha1) in Bragg-Brentano $\theta/2\theta$ geometry and with Cu K α 1 radiation.

Electrochemical analysis

The prepared cells were placed inside an in-house built apparatus for the electrochemical investigation. Two platinum nets were applied on both the WE and CE surfaces in order to optimize the electrical contacts. The system was heated at a rate of 0.9 °C min⁻¹ up to the testing temperature. The measurements were carried out in two- and three-electrode configuration, using a potentiostat coupled to a frequency response analyzer (Metrohm Autolab PGSTAT302N).

Impedance measurements were carried out in a frequency range of 10⁶ to 10⁻¹ Hz in potentiostatic mode. Before starting any systematic analysis, the linearity of the current response to the input voltage perturbation was checked. This was verified by ranging the voltage perturbation amplitude from 5 to 50 mV and checking if the current

perturbation was varying linearly with the voltage perturbation [18]. Short circuit measurements of the cell rig were performed under the same conditions of the impedance analysis and the obtained data were used to correct inductance in the impedance spectra [19].

The measurements were collected between 400-700 °C. Impedance tests were performed both at open circuit voltage (OCV) and at applied cathodic and anodic overpotential up to ± 0.2 V versus OCV, in order to study the oxygen electrode in both conditions: oxygen reduction and oxygen evolution. The impedance results were analyzed using an in-house DRT [20] code and ZView software package.

To test the stability of the systems an aging procedure was followed for more than 100 hours alternating a current load of ± 0.2 A·cm⁻² at the cell in the two-electrode configuration.

RESULTS AND DISCUSSION

Porous Electrolyte Backbone

The described procedure used to prepare the electrolyte support allowed to obtain a porous/dense/porous symmetrical structure. The porous scaffolds on the top of the dense pellet presents a homogeneous porosity distribution with a 40 % porosity, analyzed using ImageJ software, and thickness ranging between 12 and 20 μm . **Figure 2** shows the cross section on one side of the electrolyte support. The one-step sintering of the cold pressed pellet and screen-printed electrolyte ink resulted in the formation of a very robust electrolyte/electrode interface that can withstand the mechanical stresses

arising from gas evolution when SOC is operating in reverse mode and at high current densities.

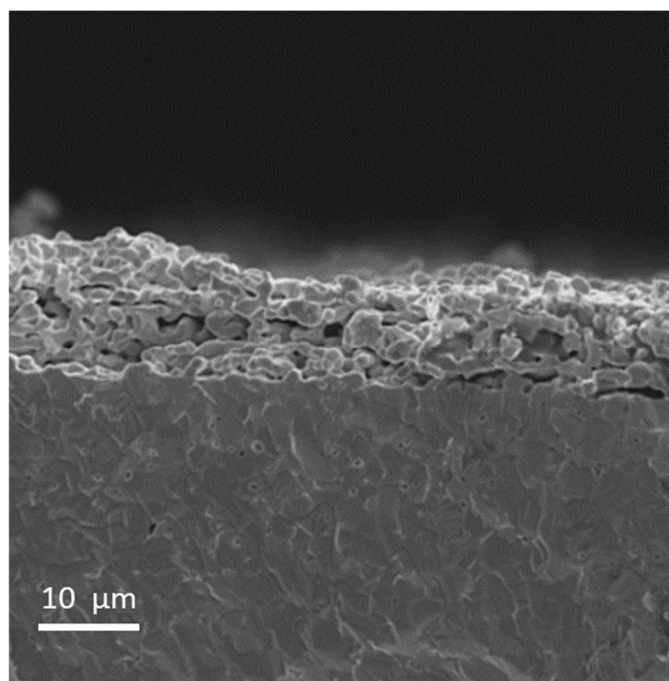


Figure 2 Cross-section SEM image of the porous backbone showing the thickness achieved by screen-printing technique.

The SDC porous layer morphology is also observable from its top view in **Figure 3 (a)**. The spherical graphite particles used as pore-former led to a pore size distribution ranging in a window of few microns (1.5 - 4 μm), suitable to host the active electrocatalyst. Moreover, **Figure 3 (b)** shows a well delimited boundary of this circular porous electrolyte layer that allows a reproducible geometry, useful for the estimation of the apparent electrodic active surface.

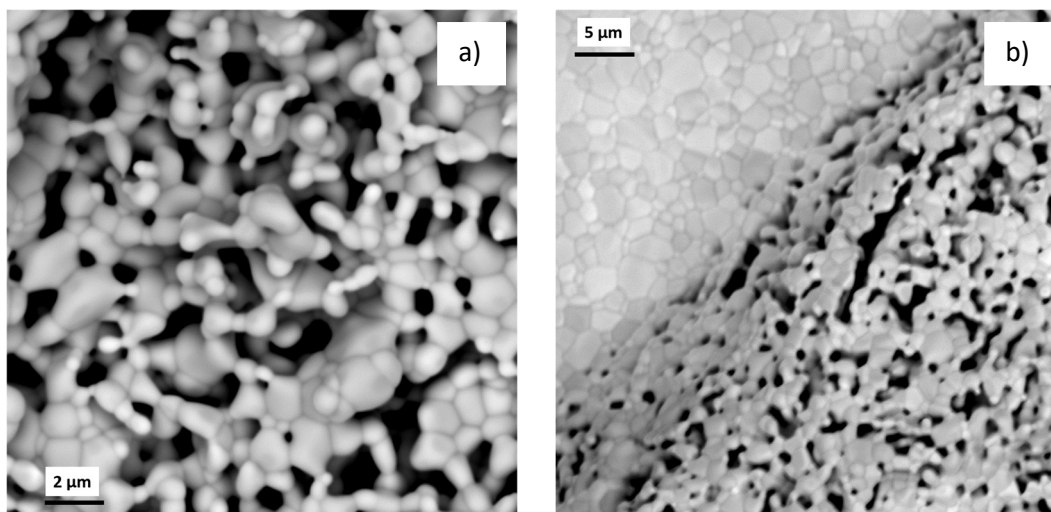


Figure 3 Top-view SEM images of the porous backbone showing **(a)** pore homogeneity and connectivity and **(b)** boundary of dense electrolyte and porous area.

Morphological and structural characterization

Figure 4 shows SEM micrographs of the studied symmetrical cells infiltrated with different loadings. It can be pointed out that, the higher the loading the better is the electrocatalyst coverage of the SDC porous backbone. The shape of the structure progressively turns from the rounded crystals of the SDC backbone to the acicular of the new loaded phase. The dominating acicular structure reported in **Figure 4 (c)** highlights that with the 20% of electrocatalyst loading a complete coverage of the porous electrolyte backbone is obtained. With this infiltration load, a sufficiently open electrode structure is however maintained. This last aspect is relevant especially considering the typical operating conditions of SOECs working at high current densities.

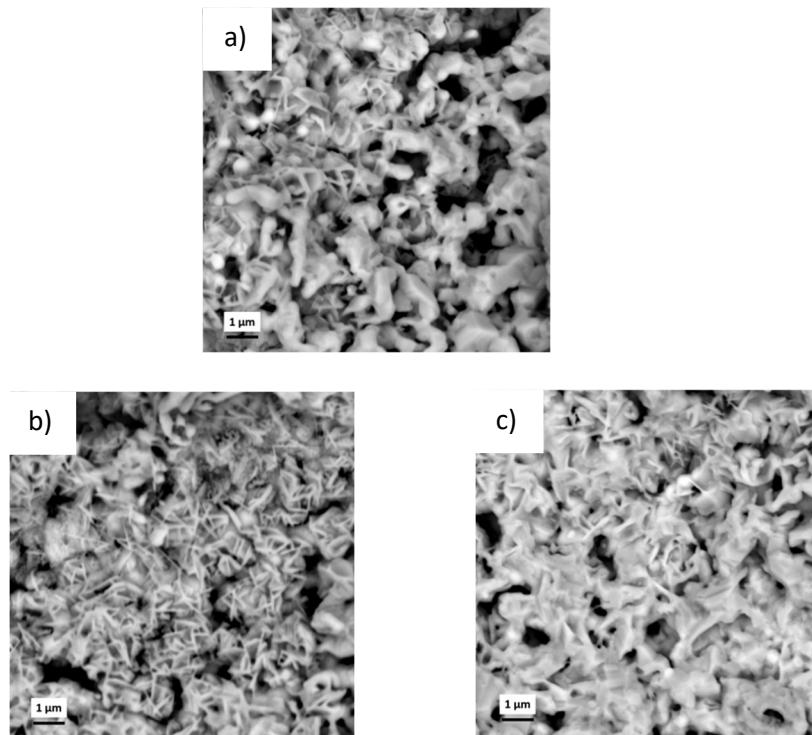


Figure 4 Top-view SEM images (a), (b) and (c) of the infiltrated backbone resulting in 10, 15 and 20 wt.% of electrocatalyst, respectively.

Figure shows an EDX mapping of Ba, Sr, Co and Fe along the electrode cross-section of an electrode after ageing. The maps show a good penetration of infiltrated elements in the whole scaffold volume, as well as their quite homogeneous spatial distribution.

The phase composition of infiltrated electrodes was investigated by XRD carried out after calcination at 850 °C. The analyses indicate the formation of the expected BSCF phase with cubic structure but also the presence of other BSCF-based oxides phases with cubic and tetragonal symmetry that can be formed during thermal treatment, possibly including Ce and Sm atoms diffusing from the SDC scaffold.

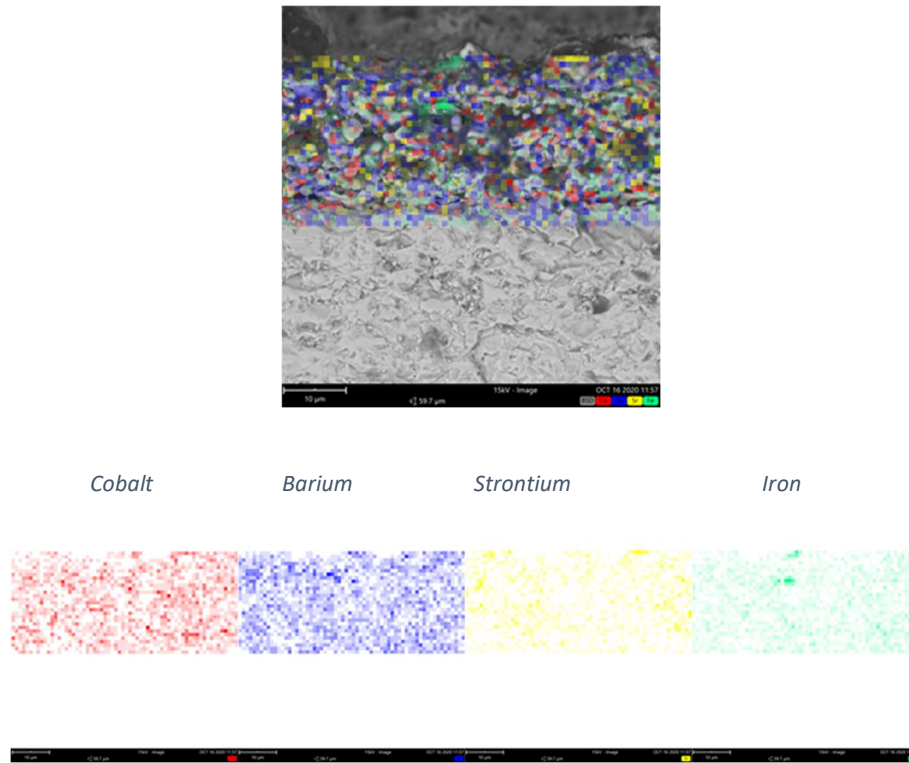


Figure 5 cross-section SEM image and EDX mapping of the infiltrated electrode (20% electrocatalyst loading)

Figure 6 shows, as an example, the XRD profile in the 26-34° 2θ range where two peaks from the cubic (F m -3 m) $\text{Ce}_{0.8}\text{Sm}_{0.2}\text{O}_{3-\delta}$ structure and one from the cubic (P m -3 m) $\text{Ba}_{0.5}\text{Sr}_{0.5}\text{Co}_{0.8}\text{Fe}_{0.2}\text{O}_{3-\delta}$ are visible. In addition, some broader peaks are present that are compatible with a few cubic, tetragonal or hexagonal structures with variable compositions which may be originated by partial decomposition of BSCF [21] but also by reaction with the SDC. Some reactivity between BSCF and SDC was reported [22] at $T > 900$ °C leading to the formation of $(\text{Ba,Sr,Ce,Sm})(\text{Co,Fe})\text{O}_{3-\delta}$, that is through incorporation of some Ce and Sm in the A site of the perovskite structure of BSCF. Such composition has high conductivity and its formation was believed beneficial for the performance of SOFC. Similarly, Sm-doped BaCeO_3 was formed after calcination at 900 °C for 100 h and Ba oxides were detected at the BSCF-SDC interface after cathodic polarization [23]. The determination of composition and relative amount of such

secondary phases could not be achieved due to limited resolution limit of the instrumentation available in our laboratory, however electrochemical studies indicate that their formation is not limiting the performances of electrodes.

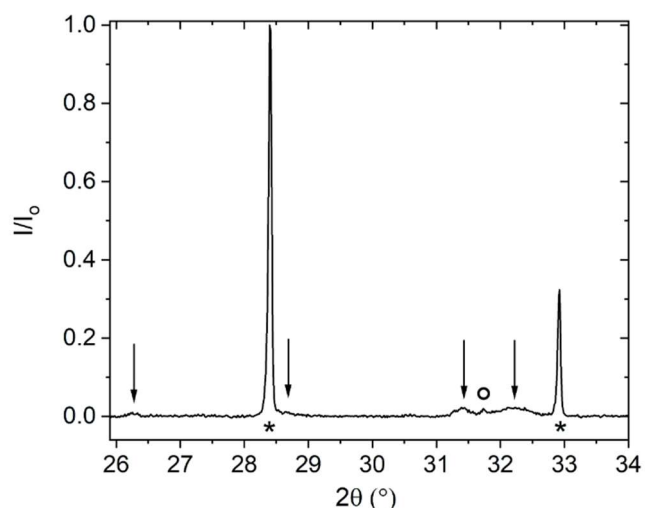


Figure 6 XRD profile of impregnated scaffold after calcination. Peaks from cubic SDC (*), cubic BSCF (°) and other intermediate phases (arrows, see text) are indicated.

Electrochemical characterization

Symmetrical cells in the configuration BSCF-SDC/SDC/BSCF-SDC, with different infiltration loadings, were investigated via Electrochemical Impedance Spectroscopy (EIS) under open circuit voltage (OCV), in air atmosphere in order to analyze how the electrocatalyst loading affects the electrochemical performance. **Figure 7** shows the Nyquist plots at OCV in the 1 MHz-0.1 Hz frequency range for BSCF-SDC/SDC/BSCF-SDC symmetric cells infiltrated with 10, 15 and 20 wt.% of BSCF at 450 °C. The result highlights that the highest electrocatalyst loading shows the fastest oxygen redox kinetic. Doubling the percentage of BSCF, from 10 to 20 wt. %, the electrode polarization resistance drastically decreases. Furthermore, considering that the thickness of the

dense electrode is constant in all the samples, it must be stressed that the BSCF loading also affects the impedance values at high frequency, which is ascribed to the cell ohmic losses. At 450 °C the electronic conductivity of BSCF is at least one order of magnitude higher than its ionic conductivity and that of SDC [24-26]. The increase of the electrocatalyst loading results in rising the number of active sites and their interconnections. Consequently, in the 20 wt.% BSCF loading, the complete coverage of the porous structure, concentrates the electrochemical reaction close to the electrode electrolyte interface. In other words, the path for the electrons is effective throughout the whole electrode thickness and oxygen ions are exchanged where their movement is easier with limited voltage loss, then, at the electrode electrolyte interface. The electrode is anyway ready to progressively extend the reaction zone in its thickness activating new reaction sites and alternative ionic paths to be used when from open circuit voltage condition a net current flow is imposed (electrolysis mode) or allowed (fuel cell mode).

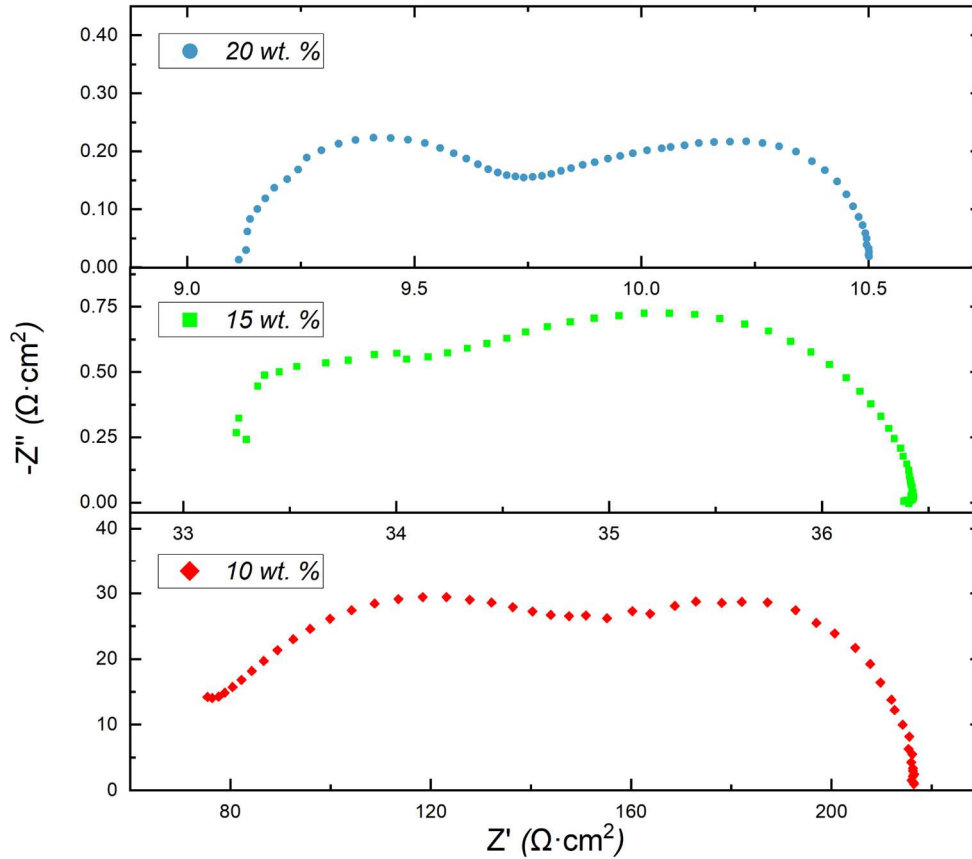


Figure 7 OCV-Nyquist plots in the 1 MHz-0.1 Hz frequency range for BSCF-SDC/SDC/BSCF-SDC symmetric cells infiltrated with 10, 15 and 20 wt.% at 450°C.

For the best performing sample, the EIS analysis in a wide temperature range (400-700 °C) was carried out (**Figure 8**). The shape of the spectra suggests the presence of at least three main processes with well separated relaxation times. Each process is thermally activated and the one related to the lower frequency range appears very sensitive to temperature variation, turning from being the controlling step at 400 °C to the non-limiting at 700 °C.

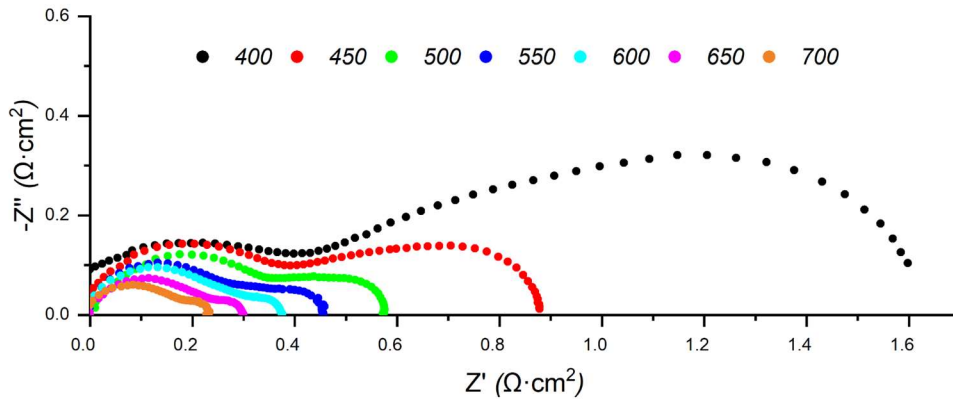


Figure 8 Impedance spectra of the symmetrical cell consisting of the 20 wt. % infiltrated BSCF; measured under OCV in the 400-700 °C temperature range where the electrolyte resistance has been removed.

The obtained R_p values are in the same magnitude range with the few ones reported in the literature regarding different electrocatalyst infiltration into a SDC backbone [27, 28]. In both cases, our electrode proposal shows higher performance at low temperature. At 500 °C we reported $0.57 \Omega \cdot \text{cm}^2$ while Xu et al. [27] reported $1 \Omega \cdot \text{cm}^2$ for a LSCF infiltrated electrode. In addition, at 550 °C we reported $0.46 \Omega \cdot \text{cm}^2$ while Wang et al. [28] reported $0.55 \Omega \cdot \text{cm}^2$ for a SSC infiltrated electrode. As it can be noticed, an increasing of temperature has a higher impact on the LSCF and SSC infiltrated electrodes and, therefore, a lower R_p value is reported. This fact could be associated to the difference between the electrode microstructure from the cited works (nanoparticles) which is much different from the one reported here (continuous nano-size layer).

Furthermore, the analysis of the distribution of the relaxation times of the processes involved in the overall reaction was performed to support the equivalent circuits modelling. **Figure** reports the distribution of relaxation times corresponding to the impedance spectra of the cell as a function of temperature from the 400 to 700 °C with $p\text{O}_2=0.21$ atm. As it can be seen in **Figure 9**, three main peaks can be identified. In

addition, as the temperature is increased, the magnitude of the peaks decreases confirming the presence of at least three thermally activated processes as expected from the Nyquist plots. Moreover, since the processes are thermally activated, it can be observed that the specific frequency increases with temperature, demonstrating a faster process. Since low frequency peak is much more affected by temperature, as the temperature is increased the low frequency peak progressively covers the mid frequency one, identified in the whole temperature range by a shoulder between 10^2 - 10^3 Hz.

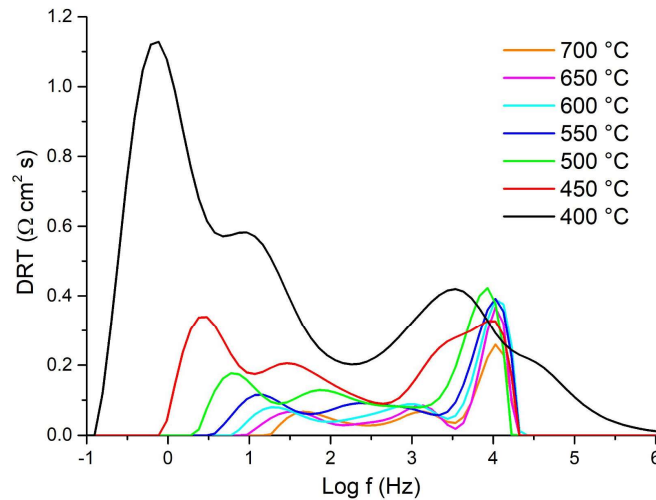


Figure 9 DRT analysis for 20 wt. % BSCF infiltrated symmetrical cell between 400-700 °C, OCV, 21% O₂

These preliminary results suggest modelling the experimental data with three sub-circuits in the equivalent circuit analysis. The circuit elements have been selected based on the shape of DRT curves. **Figure 10** proposes the DRT and the phase shift for the test at 600 °C, to highlight the features considered during the pre-screening process.

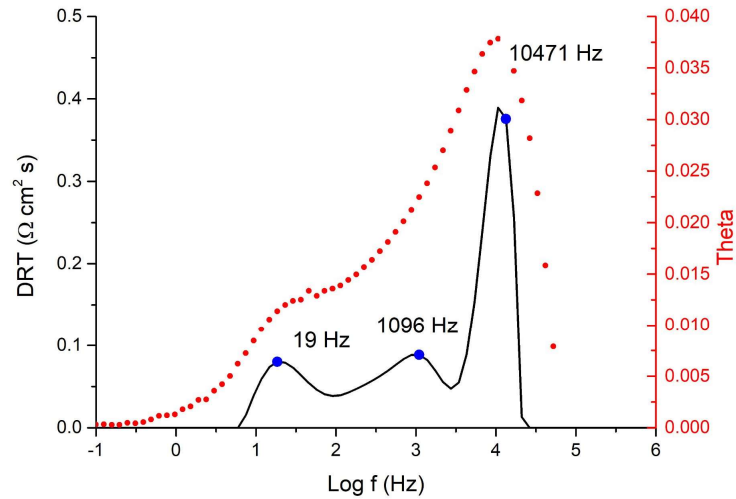


Figure 10 Comparison between Bode's diagram (dot red line), DRT (black line) and characteristic frequencies from equivalent circuit data modelling (blue points) for the 20 wt. % BSCF infiltrated symmetrical cell at 600 °C, OCV, 21% O₂

Firstly, the comparison between the phase shift (red dots) and the black curve representing the DRT confirms the good process detection thanks to the deconvolution of EIS data. This is well evident both at high frequency and by the agreement between the two peaks at medium and low frequency, where the single shoulder of Bode plot is decomposed in two contributions.

The authors are aware that matching the characteristic frequency with the processes involved is extremely tough and not unique due to the system complexity and the sensitivity of phenomena to geometries, microstructural parameters and operating conditions [29]. Nevertheless, some preliminary hypothesis about the nature of processes involved are proposed:

- the medium frequency peak (1096 Hz) and the high frequency peak (10500 Hz) show a higher skewness. In particular, the MF peak is more spread suggesting a diffusion oxygen process [30],

- the low frequency peak (19 Hz) is quite symmetric and the distortion on the right side can be attributed to the middle-frequency arc. This suggests a behavior close to an ideal capacitance [30].

Based on these considerations, an equivalent circuit (EC) made by $R_{el}(RQ)_{HF}(RQ)_{MF}(RQ)_{LF}$ is proposed in the following analysis, being Q constant phase elements at high, intermediate and low frequencies, respectively. The robustness of such choice is confirmed by the results reported in Figures 10-11-12. In **Figure 10** the characteristic frequencies for the three sub-circuits obtained with the EC data modelling analysis are also included (blue points). These characteristic frequencies are in very good agreement with the peaks provided by DRT. The accuracy of the EC fitting has been good in all the explored temperature range and **Figure** reports an example at 600 °C.

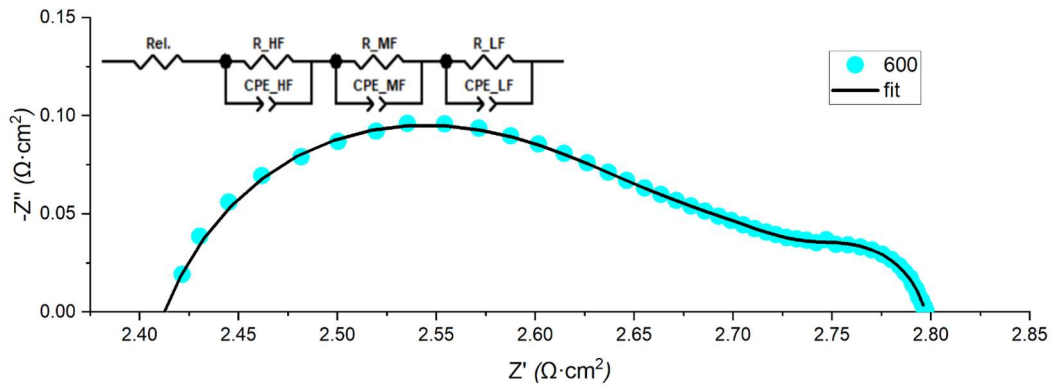


Figure 11 Experimental data and fitting of 20 wt. % infiltrated sample at 600 °C, OCV, 21% O₂.
Inset: Equivalent circuit model used to fit the experimental data

Figure 12, shows the comparison between the DRT analysis and the characteristic frequencies of all the three processes collected from the EC data modelling. Good confidence of DRT and EC analysis is confirmed in the whole temperature range. The not perfect matching at MF and HF can be attributed to the mutual interference produced

by the CPEs that deviate from a pure capacitance. Indeed, when n_{CPE} (CPE coefficient) moves away from the ideal capacitance value ($n_{CPE} = 1$), the frequency distribution becomes more spread and can affect the evaluation of the characteristic frequency of next circuit elements [20, 30]. In this specific case, both n_{HF} and n_{MF} are always lower than 0.85 ($0.84 < n_{HF} < 0.53$; $0.66 < n_{MF} < 0.57$), and such values can explain the difference between DRT and EC characteristic frequency. Moreover, from the values of n_{HF} and n_{MF} it is possible to ascribe the medium-high part of the impedance to diffusion processes.

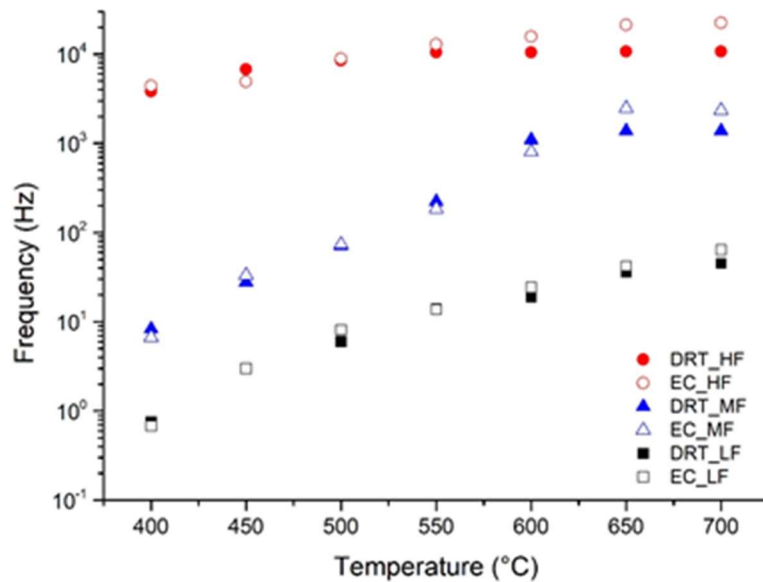


Figure 12 Comparison between characteristic frequencies from DRT (filled symbols) and from Equivalent Circuit analysis (empty symbols).

Regarding the low-frequency process the n_{LF} parameter is close to unity ($0.93 < n_{LF} < 0.99$), which suggests a process related to the charge transfer of oxygen reaction [13, 31].

The EC data fitting provides the values of polarization resistance, which allows further calculation of the global activation energy (**Figure 2**). The diagram displays a kink at

about 500 °C that underlines a change of the controlling regime in the overall oxygen reaction process. Below 500 °C, the obtained activation energy (0.46 eV) is mainly determined by the electrochemical charge transfer step, according with the dominating weight of the low frequency loop in the impedance plots at T below 500 °C (Fig. 8). Above 500 °C the electrocatalyst is ready to rapidly exchange electrons but the transport phenomena of the electroactive species starts to limit the overall reaction, the medium and high frequency loops contribution dominate in the overall impedance plot, and the obtained value for the activation energy decreases (0.25 eV).

The obtained activation energies are lower than values proposed in literature for perovskite-based bulk electrode (1.10-1.50 eV) [11, 32] and for Sm-doped ceria electrolytes (0.8 eV) [33] respectively, which indicate faster ORR kinetics at lower temperature.

Nevertheless, the features of the SDC scaffold coupled with BSCF infiltration could explain this discrepancy. Such structure provides a very tiny, well-dispersed and active BSCF phase for oxygen reaction at gas-electrode interface. Moreover, the continuity of the SDC grains within the porous and the dense electrolyte provide a very good ionic interconnection. This combination is likely to justify the obtained low values of the global activation energies.

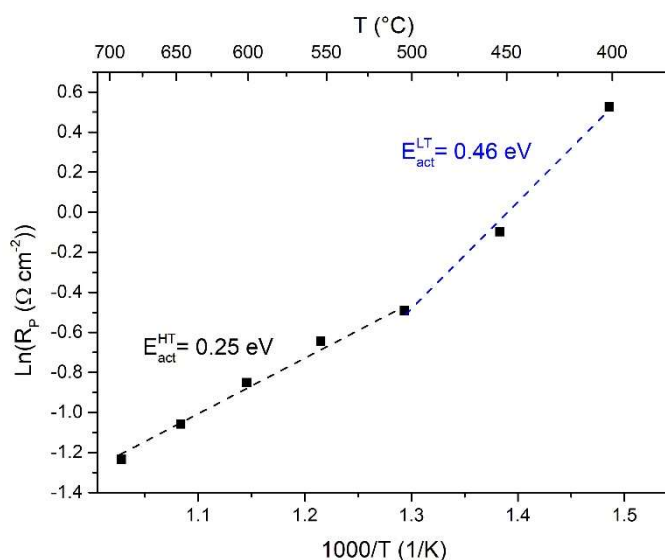


Figure 2 Arrhenius plot and activation energy for the 20 wt. % infiltrated sample between 400 – 700 °C, 21% O₂.

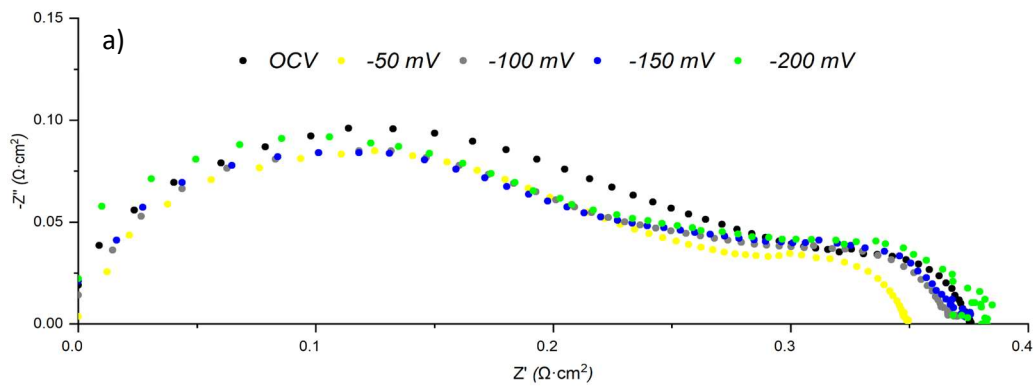
It is worth noting that the obtained values of the polarization resistances (i.e. 0.42 Ω cm² @600 °C) are slightly higher compared to the best results reported in literature for BSCF-based electrode (around 0.15 Ω cm² @600°C [32, 34]). This suggests that the electrode system proposed is suitable for the ORR but requires further electrode architecture optimization. However, the presented very low global activation energies underline that the system kinetic well cope with temperature lowering.

Overpotential effects

Working with mixed ionic-electronic compounds it is relevant to explore how they behave under polarization. In this case, being the considered system oriented to a reversible operating mode, the applied overpotentials range in the anodic and cathodic zones. **Figure 3** reports the Nyquist plots and the related DRT analysis for the 20 wt. % BSCF infiltrated electrode (in its three-electrode configuration) under anodic and cathodic polarization at 600 °C. The effect of the anodic overpotentials produces a slight

decrease of the overall polarization resistance of the system which is in agreement with literature [35]. On the other hand, when the electrode is subjected to cathodic polarization, the impedance spectra displays a rather constant behavior and the corresponding DRT analysis confirms such a trend; the processes involved are identified with the same relaxation times (Figure 14).

In previous works [36, 37], it has been demonstrated that BSCF cathodically polarized shows a decrease of its ionic conductivity due to clustering of lattice oxygen defects. The results here reported highlight that such phenomenon is inhibited in the thin BSCF layer deposited on the SDC backbone. These results confirm that under load, in both electrolysis and fuel cell mode, the electrode works without adding losses.



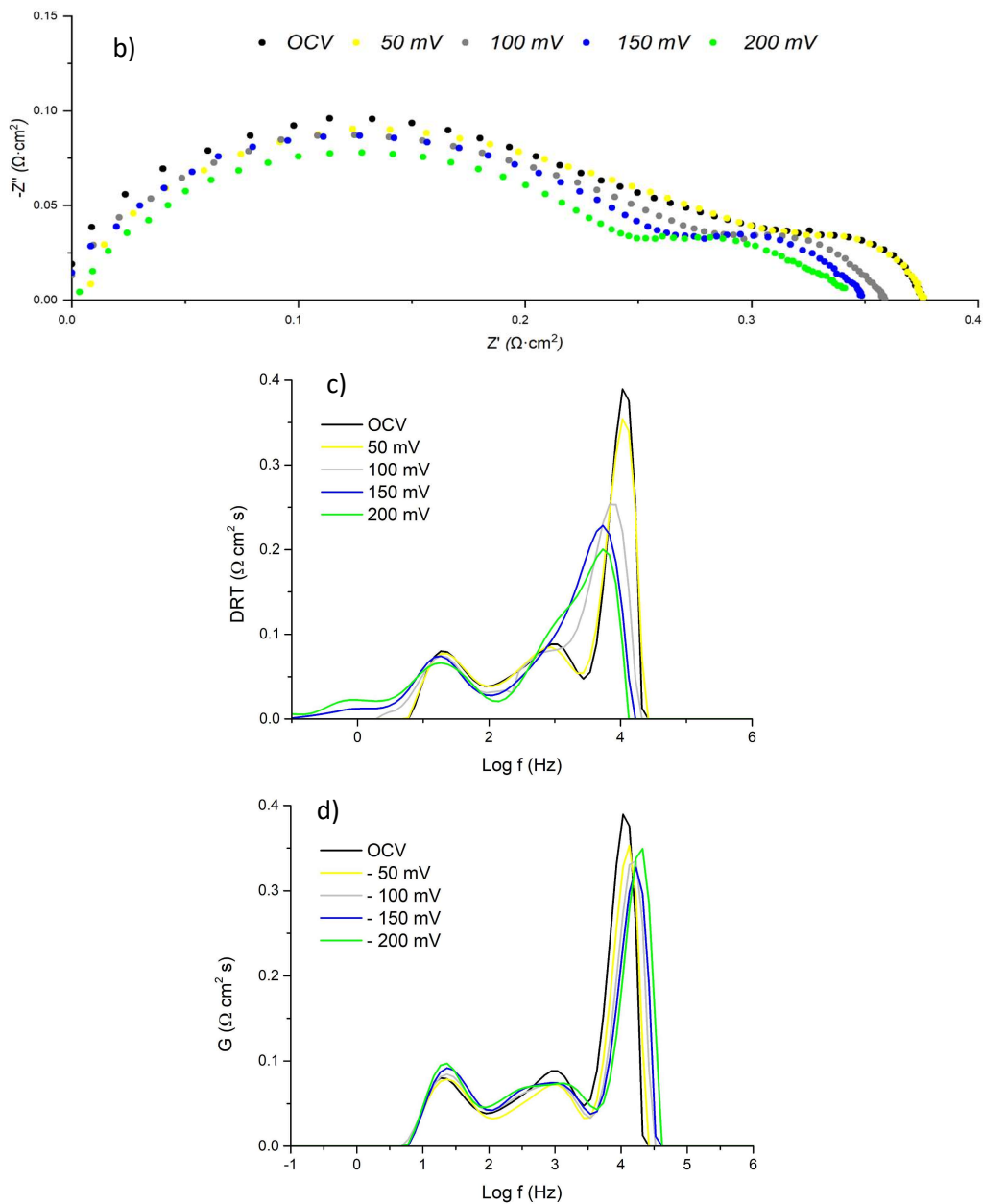


Figure 34 Impedance spectra of the 20 wt. % BSCF infiltrated symmetrical cell at (a) anodic and (b) cathodic overpotentials at 600 °C and c), d) related DRT analysis.

Ageing test

The electrochemical characterization has been completed checking the stability on the electrodic activity when subjected to an aging test. The stability of the electrode is the first issue of any system once the sought performances are achieved. It is well established that in the first hundred hours electrode materials display the most relevant

activity decay [32, 38]. Consequently, the symmetrical cells have been subjected to an alternating ORR and OER regime at constant current load of $200 \text{ mA}\cdot\text{cm}^{-2}$ in air at $600 \text{ }^\circ\text{C}$ switching the current every 24 hours. Before any current switch impedance at OCV was recorded. **Figure 4** shows the results registered for the 20 wt. % infiltrated BSCF sample. The system is fully stable in the timescale considered and when it is subjected to the oxygen reduction regime an activation of the electrode is occurring. Such alternating conditions constitute a significant source of degradation processes; however, the good response of the studied system sets the premises for a robust and reliable air electrode also in harsh conditions.

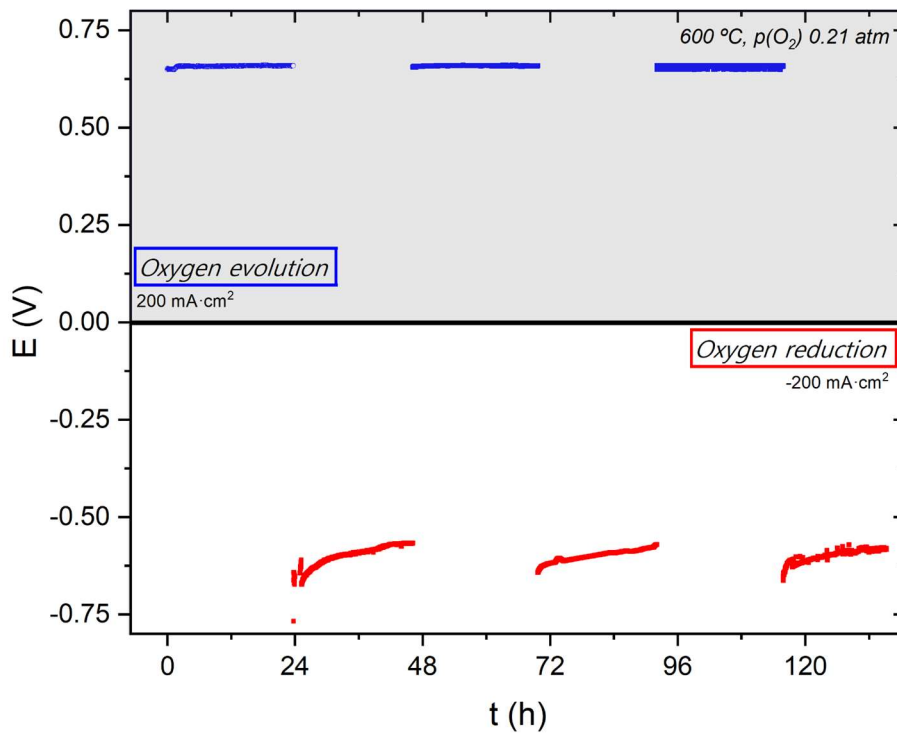


Figure 4 Ageing test under anodic and cathodic polarization for 20 wt. % BSCF infiltrated symmetrical cell.

The results highlight how the reported electrode architecture could potentially open a new way of exploiting BSCF electrocatalytic properties and avoiding the typical instability issue related to this material.

Conclusions

In summary, the present work demonstrates how the proposed modification of the microstructure of the air electrode potentially overcome some of the main issues regarding solid oxide cells durability. The described electrode shaping procedure is viable for upscaling. However, electrolyte cold pressing should be replaced by tape casting and electrocatalyst precursor infiltration has to be performed by wet spraying or deep coating in order to achieve a full scalable manufacture procedure.

The proposed methodology to synthesize the electrocatalyst inside the porous electrolyte backbone successfully produces a well-dispersed active phase which covers the whole backbone with a thin-film coating. This nano-sized thin-film coating and the good link of the electrocatalyst with the robust electrolyte porous structure highlights material peculiar properties well beyond that those typically achieved with traditional composite electrodes. In particular, the modified air electrode synergistically enhances ORR and OER showing no oxygen vacancies clustering under current load, which typically induces an increase of the electrode polarization resistance. Furthermore, the obtained overall activation energy of the process is dramatically decreased as a result of a **drastic** change of the reaction mechanism.

The prepared system has a very high stability within the considered time scale, where typically the greater degradation occurs. Although the electrochemical activity of the studied air electrode is already good, there is still room for improvements playing with the thickness and the porosity of the electrolyte backbone. Finally, the proposed electrode architecture is suitable for hosting different electrocatalysts, these are aspects that will be the subject of further investigations by the authors.

Acknowledgements

This work was partially supported by the Project “COELUS: Production of renewable fuel by CO-Electrolysis and reUse of carbon dioxide” funded by the Compagnia di San Paolo, under the ROL ID:32604.

References

- [1] Glanemann N, Willner SN, Levermann A. Paris Climate Agreement passes the cost-benefit test. *Nature Communications*. 2020;11(1):110.
- [2] van Soest HL, den Elzen MGJ, van Vuuren DP. Net-zero emission targets for major emitting countries consistent with the Paris Agreement. *Nature Communications*. 2021;12(1):2140.
- [3] Hauch A, Kungas R, Blennow P, Hansen AB, Hansen JB, Mathiesen BV, et al. Recent advances in solid oxide cell technology for electrolysis. *Science*. 2020;370(6513):eaba6118.
- [4] Mahmood A, Bano S, Yu JH, Lee K-H. High-performance solid oxide electrolysis cell based on ScSZ/GDC (scandia-stabilized zirconia/gadolinium-doped ceria) bi-layered electrolyte and LSCF (lanthanum strontium cobalt ferrite) oxygen electrode. *Energy*. 2015;90:344-50.

- [5] Chen G, Wang Y, Sunarso J, Liang F, Wang H. A new scandium and niobium co-doped cobalt-free perovskite cathode for intermediate-temperature solid oxide fuel cells. *Energy*. 2016;95:137-43.
- [6] Lee Y-L, Kleis J, Rossmeisl J, Shao-Horn Y, Morgan D. Prediction of solid oxide fuel cell cathode activity with first-principles descriptors. *Energy & Environmental Science*. 2011;4(10):3966-70.
- [7] Mastrikov YA, Merkle R, Kotomin EA, Kuklja MM, Maier J. Formation and migration of oxygen vacancies in $\text{La}_{1-x}\text{Sr}_x\text{Co}_{1-y}\text{Fe}_y\text{O}_{3-\delta}$ perovskites: insight from ab initio calculations and comparison with $\text{Ba}_{1-x}\text{Sr}_x\text{Co}_{1-y}\text{Fe}_y\text{O}_{3-\delta}$. *Physical Chemistry Chemical Physics*. 2013;15(3):911-8.
- [8] Sunarso J, Baumann S, Serra JM, Meulenber WA, Liu S, Lin YS, et al. Mixed ionic-electronic conducting (MIEC) ceramic-based membranes for oxygen separation. *Journal of Membrane Science*. 2008;320(1):13-41.
- [9] Vázquez S, Suescun L, Faccio R. Effect of Cu doping on $\text{Ba}_{0.5}\text{Sr}_{0.5}\text{Fe}_{1-x}\text{Cu}_x\text{O}_{3-\delta}$ perovskites for solid oxide fuel cells: A first-principles study. *Journal of Power Sources*. 2016;311:13-20.
- [10] Müller P, Störmer H, Dieterle L, Niedrig C, Ivers-Tiffée E, Gerthsen D. Decomposition pathway of cubic $\text{Ba}_{0.5}\text{Sr}_{0.5}\text{Co}_{0.8}\text{Fe}_{0.2}\text{O}_{3-\delta}$ between 700°C and 1000°C analyzed by electron microscopic techniques. *Solid State Ionics*. 2012;206:57-66.
- [11] Gao Z, Mogni LV, Miller EC, Railsback JG, Barnett SA. A perspective on low-temperature solid oxide fuel cells. *Energy & Environmental Science*. 2016;9(5):1602-44.
- [12] Liu D, Dou Y, Xia T, Li Q, Sun L, Huo L, et al. B-site La, Ce, and Pr-doped $\text{Ba}_{0.5}\text{Sr}_{0.5}\text{Co}_{0.7}\text{Fe}_{0.3}\text{O}_{3-\delta}$ perovskite cathodes for intermediate-temperature solid oxide fuel cells: Effectively promoted oxygen reduction activity and operating stability. *Journal of Power Sources*. 2021;494:229778.

- [13] Adler SB. Factors Governing Oxygen Reduction in Solid Oxide Fuel Cell Cathodes. *Chemical Reviews*. 2004;104(10):4791-844.
- [14] Ding X, Zhu W, Gao X, Hua G, Li J. Enhanced SOFC cathode performance by infiltrating Ba_{0.5}Sr_{0.5}Co_{0.8}Fe_{0.2}O_{3-δ} nanoparticles for intermediate temperature solid oxide fuel cells. *Fuel Processing Technology*. 2015;135:14-9.
- [15] Lauret H, Hammou A. Localization of oxygen cathodic reduction zone at lanthanum manganite/zirconia interface. *Journal of the European Ceramic Society*. 1996;16(4):447-51.
- [16] Jiang SP. Nanoscale and nano-structured electrodes of solid oxide fuel cells by infiltration: Advances and challenges. *International Journal of Hydrogen Energy*. 2012;37(1):449-70.
- [17] Cimenti M, Co AC, Birss VI, Hill JM. Distortions in Electrochemical Impedance Spectroscopy Measurements Using 3-Electrode Methods in SOFC. I – Effect of Cell Geometry. *Fuel Cells*. 2007;7(5):364-76.
- [18] Macdonald JR, Johnson WB. *Fundamentals of Impedance Spectroscopy*. Impedance Spectroscopy 2005. p. 1-26.
- [19] Raikova G, Carpanese MP, Stoyanov Z, Vladikova D, Viviani M, Barbucci A. Inductance correction in impedance studies of solid oxide fuel cells. *Bulg Chem Commun*. 2009;41:199-206.
- [20] Clematis D, Presto S, Carpanese MP, Barbucci A, Deganello F, Liotta LF, et al. Distribution of Relaxation Times and Equivalent Circuits Analysis of Ba_{0.5}Sr_{0.5}Co_{0.8}Fe_{0.2}O_{3-δ}. *Catalysts*. 2019;9(5):441.
- [21] Müller P, Störmer H, Meffert M, Dieterle L, Niedrig C, Wagner SF, et al. Secondary Phase Formation in Ba_{0.5}Sr_{0.5}Co_{0.8}Fe_{0.2}O_{3-d} Studied by Electron Microscopy. *Chemistry of Materials*. 2013;25(4):564-73.

- [22] Wang K, Ran R, Zhou W, Gu H, Shao Z, Ahn J. Properties and performance of Ba_{0.5}Sr_{0.5}Co_{0.8}Fe_{0.2}O_{3-δ}+Sm_{0.2}Ce_{0.8}O_{1.9} composite cathode. *Journal of Power Sources*. 2008;179(1):60-8.
- [23] Yung H, Jian L, Jiang SP. Polarization Promoted Chemical Reaction between Ba_{0.5}Sr_{0.5}Co_{0.8}Fe_{0.2}O_{3-δ}Cathode and Ceria Based Electrolytes of Solid Oxide Fuel Cells. *Journal of The Electrochemical Society*. 2012;159(11):F794-F8.
- [24] Bucher E, Egger A, Ried P, Sitte W, Holtappels P. Oxygen nonstoichiometry and exchange kinetics of Ba_{0.5}Sr_{0.5}Co_{0.8}Fe_{0.2}O_{3-δ}. *Solid State Ionics*. 2008;179(21):1032-5.
- [25] Jung J-I, Mixture ST, Edwards DD. The electronic conductivity of Ba_{0.5}Sr_{0.5}Co_xFe_{1-x}O_{3-δ}(BSCF: x = 0 ~ 1.0) under different oxygen partial pressures. *Journal of Electroceramics*. 2010;24(4):261-9.
- [26] Zhan Z, Wen T-L, Tu H, Lu Z-Y. AC Impedance Investigation of Samarium-Doped Ceria. *Journal of The Electrochemical Society*. 2001;148(5):A427.
- [27] Xu H, Zhang H, Chu A. An investigation of oxygen reduction mechanism in nano-sized LSCF-SDC composite cathodes. *International Journal of Hydrogen Energy*. 2016;41(47):22415-21.
- [28] Wang F, Chen D, Shao Z. Sm_{0.5}Sr_{0.5}CoO_{3-δ}-infiltrated cathodes for solid oxide fuel cells with improved oxygen reduction activity and stability. *Journal of Power Sources*. 2012;216:208-15.
- [29] Caliandro P, Nakajo A, Diethelm S, Van herle J. Model-assisted identification of solid oxide cell elementary processes by electrochemical impedance spectroscopy measurements. *Journal of Power Sources*. 2019;436:226838.
- [30] Boukamp BA. Fourier transform distribution function of relaxation times; application and limitations. *Electrochimica Acta*. 2015;154:35-46.

- [31] Ascolani-Yael J, Montenegro-Hernandez A, Garcés D, Liu Q, Wang H, Yakal-Kremiski K, et al. The oxygen reduction reaction in solid oxide fuel cells: from kinetic parameters measurements to electrode design. *J Phys Energy*. 2020;2.
- [32] Clematis D, Barbucci A, Presto S, Viviani M, Carpanese MP. Electrocatalytic activity of perovskite-based cathodes for solid oxide fuel cells. *International Journal of Hydrogen Energy*. 2019;44(12):6212-22.
- [33] Presto S, Artini C, Pani M, Carnasciali MM, Massardo S, Viviani M. Ionic conductivity and local structural features in $\text{Ce}_{1-x}\text{Sm}_x\text{O}_{2-x/2}$. *Physical Chemistry Chemical Physics*. 2018;20(44):28338-45.
- [34] Almar L, Störmer H, Meffert M, Szász J, Wankmüller F, Gerthsen D, et al. Improved Phase Stability and CO₂ Poisoning Robustness of Y-Doped $\text{Ba}_{0.5}\text{Sr}_{0.5}\text{Co}_{0.8}\text{Fe}_{0.2}\text{O}_{3-\delta}$ SOFC Cathodes at Intermediate Temperatures. *ACS Applied Energy Materials*. 2018;1(3):1316-27.
- [35] Majnoni d'Intignano X, Cademartori D, Clematis D, Presto S, Viviani M, Botter R, et al. Infiltrated $\text{Ba}_{0.5}\text{Sr}_{0.5}\text{Co}_{0.8}\text{Fe}_{0.2}\text{O}_{3-\delta}$ -Based Electrodes as Anodes in Solid Oxide Electrolysis Cells. *Energies*. 2020;13(14):3659.
- [36] Giuliano A, Carpanese MP, Clematis D, Boaro M, Pappacena A, Deganello F, et al. Infiltration, Overpotential and Ageing Effects on Cathodes for Solid Oxide Fuel Cells: $\text{La}_{0.6}\text{Sr}_{0.4}\text{Co}_{0.2}\text{Fe}_{0.8}\text{O}_{3-\delta}$ versus $\text{Ba}_{0.5}\text{Sr}_{0.5}\text{Co}_{0.8}\text{Fe}_{0.2}\text{O}_{3-\delta}$. *Journal of The Electrochemical Society*. 2017;164(10):F3114-F22.
- [37] Giuliano A, Carpanese MP, Panizza M, Cerisola G, Clematis D, Barbucci A. Characterisation of $\text{La}_{0.6}\text{Sr}_{0.4}\text{Co}_{0.2}\text{Fe}_{0.8}\text{O}_{3-\delta}$ – $\text{Ba}_{0.5}\text{Sr}_{0.5}\text{Co}_{0.8}\text{Fe}_{0.2}\text{O}_{3-\delta}$ composite as cathode for solid oxide fuel cells. *Electrochimica Acta*. 2017;240:258-66.
- [38] Kim J-S, Yeon D-H, Jung DW, Kwak C. A highly active and long-term stable La-doped $\text{Ba}_x\text{Sr}_{1-x}\text{Co}_{1-y}\text{Fe}_y\text{O}_{3-\delta}$ cathode for solid-oxide fuel cells. *Journal of Power Sources*. 2014;249:66-71.